A Monohydrosulfido Dinitrosyl Diiron Complex Generates N_2O as a Model for Flavodiiron Nitric Oxide Reductases: Reaction Mechanism and Electronic Structure

Nabhendu Pal,[†] Corey J. White,[‡] Serhiy Demeshko,[§] Franc Meyer,[§] Nicolai Lehnert[‡] and Amit Majumdar*[†]*

[†]School of Chemical Sciences, Indian Association for the Cultivation of Science, 2A & 2B Raja S. C. Mullick Road, Kolkata 700032, West Bengal, India

[‡]Department of Chemistry, The University of Michigan, Ann Arbor 48109, Michigan, USA

[§]Universität Göttingen, Institut für Anorganische Chemie, Tammannstraße 4, Göttingen 37077, Germany

*Email: lehnertn@umich.edu; icam@iacs.res.in

ABSTRACT. Flavodiiron nitric oxide reductases (FNORs) protect microbes from nitrosative stress under anaerobic conditions by mediating the reduction of nitric oxide (NO) to nitrous oxide (N_2O). The proposed mechanism for the catalytic reduction of NO by FNORs involves a dinitrosyl diiron intermediate with [hs-$\{FeNO\}^7$]$_2$ formulation, which produces N_2O and a diferric species. Moreover, both NO and H_2S have been implicated in several similar physiological functions in biology and are also known to cross paths in cell signaling. Here we report the synthesis, spectroscopic and theoretical characterization, and N_2O production activity of an unprecedented monohydrosulfido dinitrosyl diiron compound, with a [(HS)hs-$\{FeNO\}^7$/hs-$\{FeNO\}^7$] formulation, which models the key dinitrosyl intermediate of FNORs. Generation of N_2O from this unique compound follows a semireduced pathway, where one-electron reduction generates a reactive hs-$\{FeNO\}^8$ center via occupation of an Fe-NO antibonding orbital. In contrast to the well-known reactivity of H_2S and NO, the coordinated hydrosulfide remains unreactive towards NO and acts only as a spectator ligand during the NO reduction process.

INTRODUCTION

Nitric oxide (NO) plays important roles in cardiovascular maintenance,[1] nerve signal transduction[2-4] and the immune defense mechanism of mammals against invading pathogens.[3-5] While inducible NO synthase can produce up to micromolar concentrations of NO as a response to bacterial infection,[6] few microbes such as *T. maritima*, *M. thermoacetica* and *D. gigas* express the enzyme flavodiiron nitric oxide reductases (FNORs), which reduce the toxic molecule NO to less toxic nitrous oxide (N_2O).[7-10] The FNOR activity thus protects the microbes from nitrosative stress under anaerobic conditions.[11] The active site of FNORs comprises two non-heme iron centers, each one usually coordinated by two histidines and a glutamate.[12, 13] The coordination spheres are completed by two bridging ligands: a hydroxide and an aspartate. While four different mechanisms have been proposed for the reduction of NO to N_2O by FNORs,[7-9, 12-14] a recent study has revealed that the reaction proceeds through the successive formation of mono- and di-nitrosyl diiron species, of which the latter produces N_2O.[15] Quite similar to NO, hydrogen sulfide (H_2S) has also been recognized as a possible endogenous gasotransmitter[16] and has been implicated in several physiological processes[17] such as cardiovascular effects,[18] vasodilation[19, 20] and neuromodulation.[21, 22] H_2S ($pK_a = 6.9$) remains as an equilibrium mixture of hydrosulfide (HS^-) and H_2S with a ratio of 3:1 at the biological pH of 7.4. Therefore, any or both of these two species may act as ligands for the metal ions available in biological systems. NO and H_2S have also been implicated to cross paths in cell signaling, via the formation of HNO, (H)SNO, (H)SSNO, and polysulfides.[23, 24]

Functional model complexes of FNORs include cis-dinitrosyl diiron complexes that could produce N_2O in quantitative yield either directly (by N.L.),[25] or upon reduction at room temperature (by N.L.)[26] via a semireduced mechanism[27] (by N.L. and F.M.) or upon photolysis at low temperature.[28] However, a trans-dinitrosyl diiron complex was found (by F.M.) to be ineffective towards production of N_2O.[29]

Recently, we have reported the only example of a model mononitrosyl diiron compound,[30] and its dinitrosyl analogue,[31] both of which could produce N_2O upon reduction by following the superreduced and the semireduced pathway, respectively.[31] However, the effect of co-ligands on the N_2O yield and NO reduction activity of model complexes has not been explored yet. Furthermore, despite the intriguing reactions of H_2S/HS^- with NO in biological systems, studies on the reactivity of H_2S/HS^- towards NO in non-heme diiron complexes are unavailable in the literature. Elucidating the mechanism of NO reduction by FNORs as well as understanding the interaction of NO with H_2S/HS^- in functional non-heme diiron complexes is therefore of significant interest.

The reactivity of H_2S/HS^- towards NO in non heme iron complexes has been explored so far only in the context of sodium nitroprusside,[32-35] dinitrosyl and mononitrosyl iron complexes (DNICs/MNICs),[36-40] and iron-sulfur clusters,[41-46] which, however, are distinctly different classes of compounds as compared with nonheme diiron complexes. Considering the importance of the reactivity of NO with H_2S/HS^- in biology, we planned to investigate the reactivity of NO towards non-heme diiron(II)-hydrosulfide complexes in the context of FNOR activity. Recently, one of us (A.M.) has reported a series of non-heme diiron(II)-hydrosulfide complexes[47, 48] which provide an excellent opportunity for investigating the reactivity of HS^- and NO in this class of diiron complexes. Here we report the synthesis, extensive characterization and NO reduction activity of an unprecedented monohydrosulfido dinitrosyl diiron compound, $[Fe_2(N\text{-Et-HPTB})(SH)(NO)_2(DMF)](BF_4)_2$ (**1**$(BF_4)_2$) (where *N*-Et-HPTB[49] is the anion of *N*,*N*,*N*′,*N*′-tetrakis(2-(l-ethylbenzimidazolyI))-2-hydroxy-1,3-diaminopropane), which features a [(HS)hs-$\{FeNO\}^7$/hs-$\{FeNO\}^7$] formulation. To the best of our knowledge, there is no analogue with any dinucleating ligand system in the literature for the unique structural features of complex **1**.

EXPERIMENTAL SECTION

Preparation of Compounds. All reactions and manipulations were performed under a pure argon atmosphere using either standard Schlenk techniques or an inert atmosphere box. Solvents were dried following standard procedures.[50, 51] $Fe(BF_4)_2 \cdot 6H_2O$, $Fe(ClO_4)_2 \cdot xH_2O$, $Fe(OTf)_2$, Cp_2Fe, Cp_2Co, Et_3N and NaS^tBu were obtained from commercial sources and were used without further purification. H*N*-Et-HPTB[49, 52] and tritylnitrosothiol (Ph_3CSNO)[43] was prepared following the procedures reported in the literature. In the preparations that follow, all the filtrations were performed through Celite and solvent removal steps were carried out in vacuo inside an inert (argon gas) atmosphere box. Yields are for recrystallized compounds and are average of individual yields obtained from multiple batches of reactions, calculated using corresponding molecular weights of the compound shown in Table S1.

*$[Fe_2$(N-Et-HPTB)$(SH)(NO)_2(DMF)](BF_4)_2$ (**1**$(BF_4)_2$).* To a solution of [Fe_2(*N*-Et-HPTB)$(SH)(H_2O)](BF_4)_2 \cdot$DMF (**2**$(BF_4)_2 \cdot$DMF) (0.04 mmol, 53.28 mg) in 1 mL of DMF was added Ph_3CSNO (0.32 mmol, 96.0 mg) in 1 mL of DMF and stirred for 4 hours to obtain a dark green solution. The solution was filtered, and Et_2O was allowed to diffuse into the filtrate overnight at −35°C with an additional 1 day standing at r.t. to afford greenish-brown colored block-shaped crystals. The crystals were washed several times with THF and Et_2O followed by drying under vacuum to yield 38.0 mg (81%) of **1**$(BF_4)_2$. The identity of the compound obtained was confirmed by a single crystal X-ray structure determination. Anal. Calcd for: $C_{46}H_{57}B_2F_8Fe_2N_{13}O_4S_1$ (**1**$(BF_4)_2$): C, 47.09%; H, 4.90%; N, 15.52%. Found: C, 46.85%; H, 5.15%; N, 15.39%. ESI-MS in MeCN (saturated with NO): found (calcd) for [Fe_2(*N*-Et-HPTB)$(SH)(NO)_2]^{3+}$: m/z 464.1357 (464.1347). Absorption spectrum (DMF) λ_{max} (ε_M M^{-1} cm^{-1}): 342 (3450 ± 40), 525(245 ± 35), 600 (210 ± 5) nm. IR: ν_{SH} = 2516 cm^{-1} (KBr pellet). ν_{NO} = 1785 cm^{-1} (KBr pellet); 1796 cm^{-1} (in MeCN). Mössbauer: δ = 0.65 mm/s (ΔE_Q = 1.39 mm/s) at 80 K. XPS: S 2p at 162.0 eV. EPR: EPR silent at 4 K.

Alternative synthesis of ***1***$(BF_4)_2$ *using NO gas*. To a solution of [Fe_2(*N*-Et-HPTB)(SH)(H_2O)]($BF_4)_2$·DMF (**2**($BF_4)_2$·DMF) (0.04 mmol, 53.28mg) in 2 mL of DMF, NO gas was added (purged) for 2 minutes. The solution was filtered, and Et_2O was allowed to diffuse into the filtrate overnight at −35°C with an additional 1 day standing at r.t. to afford greenish-brown colored blockshaped crystals. The crystals were washed several times with THF and Et_2O followed by drying under vacuum to yield 40.2 mg (85%) of of **1**($BF_4)_2$. The identity of the compound obtained was confirmed by a single crystal X-ray structure determination and IR spectroscopy.

[Fe_2*(N-Et-HPTB)(SH)*$(NO)_2$*(DMF)](*$ClO_4)_2$ *(****1****(*$ClO_4)_2$*).* To a mixture of H*N*-Et-HPTB (0.08 mmol, 57.8 mg), Et_3N (0.12 mmol, 12.1 mg) and NaS^tBu (0.12 mmol, 15 mg) in 2 mL of DMF was added $Fe(ClO_4)_2·6H_2O$ (0.16 mmol, 58.0 mg) with stirring, and the resultant slurry was stirred for 6h. The reaction mixture was filtered. Et_2O was added into the filtrate to afford [Fe_2(*N*-Et-HPTB)(SH)(H_2O)]($ClO_4)_2$·DMF (**2**($ClO_4)_2$·DMF) as a pale yellow solid which was used directly in the next step. To a solution of **2**($ClO_4)_2$·DMF (0.04 mmol, 54.36 mg) in 1 mL of DMF was added Ph_3CSNO (0.32 mmol, 96.0 mg) in 1 mL of DMF and stirred for 4 hours to obtain a dark green solution. The solution was filtered, and Et_2O was allowed to diffuse into the filtrate overnight at −35°C with an additional 1 day standing at r.t. to afford greenish-brown colored block-shaped crystals. The crystals were washed several times with THF and Et_2O followed by drying under vacuum to yield 37.0 mg (77%) of **1**($ClO_4)_2$. The identity of **1**($ClO_4)_2$ was confirmed by a single crystal X-ray structure determination. Anal. Calcd for: $C_{46}H_{57}Cl_2Fe_2N_{13}O_{12}S_1$·DMF·$H_2O$ (**1**($ClO_4)_2$·DMF·H_2O): C, 45.63%; H, 5.16%; N, 15.20%. Found: C, 45.38%; H, 5.59%; N, 14.88%. ESI-MS in MeCN found (calcd) for [Fe_2(*N*-Et-HPTB)(SH)$(NO)_2]^{2+}$: m/z 464.1347 (464.1347). IR (KBr pellet): ν_{SH} = 2509 cm^{-1}, ν_{NO} = 1782 cm^{-1}.

*[Fe_2(N-Et-HPTB)(SH)$(NO)_2$(DMF)]$(OTf)_2$ (**1**$(OTf)_2$).* To a mixture of H*N*-Et-HPTB (0.08 mmol, 57.8 mg), Et_3N (0.12 mmol, 12.1 mg) and NaS^tBu (0.12 mmol, 15 mg) in 2 mL of DMF was added $Fe(OTf)_2$ (0.16 mmol, 56.6 mg) with stirring, and the resultant slurry was stirred for 6h. The reaction mixture was filtered. Et_2O was added into the filtrate to afford [Fe_2(*N*-Et-HPTB)(SH)(H_2O)]$(OTf)_2$·DMF (**2**$OTf)_2$·DMF) as a pale yellow solid which was directly used in the next step. To a solution of (**2**$OTf)_2$·DMF) (0.04 mmol, 58.50 mg) in 1 mL of DMF was added Ph_3CSNO (0.32 mmol, 96.0 mg) in 1 mL of DMF and stirred for 4 hours to obtain a dark green solution. The solution was filtered, and Et_2O was allowed to diffuse into the filtrate overnight at −35°C with an additional 1 day standing at r.t. to afford greenish-brown colored block-shaped crystals. The crystals were washed several times with THF and Et_2O followed by drying under vacuum to yield 40.0 mg (74%) of **1**$(OTf)_2$. The identity of **1**$(OTf)_2$ was confirmed by a single crystal X-ray structure determination. Anal. Calcd for: $C_{48}H_{57}F_6Fe_2N_{13}O_{10}S_3$·3DMF·$Et_2O$ (**1**$(OTf)_2$·3DMF·Et_2O).: C, 46.04%; H, 5.57%; N, 14.08%. Found: C, 45.76%; H, 5.44%; N, 14.37%. ESI-MS in MeCN found (calcd) for [Fe_2(*N*-Et-HPTB)(SH)$(NO)_2$]$^{2+}$: m/z 464.1347 (464.1347). IR (KBr pellet): ν_{SH} = 2532 cm^{-1}, ν_{NO} = 1782 cm^{-1}.

*Reaction of (**1**$(BF_4)_2$* with 1 equiv of Cp_2Co. To a solution of ***1***$(BF_4)_2$ (0.085 mmol, 100 mg) in 5 mL of CH_2Cl_2 was added a solution of Cp_2Co (0.085 mmol, 16.1 mg) in 2 mL of CH_2Cl_2. The color of the solution immediately changed from greenish to dark brown. The resulting solution was stirred for 1 h and evaporated to dryness. The residue was washed twice with MeOH, dissolved in 2 mL of DMF and filtered. Et_2O was allowed to diffuse into the filtrate overnight at RT to yield a light brown crystalline solid (61 mg).

*Reaction of (**1**$(BF_4)_2$* with 2 equiv of Cp_2CO. To a solution of ***1***$(BF_4)_2$) (0.085 mmol, 100 mg) in 5 mL of CH_2Cl_2 was added a solution of Cp_2Co (0.17 mmol, 32.2 mg) in 2 mL of CH_2Cl_2. The color of

the solution immediately changed from greenish to dark brown. The resulting solution was stirred for 1 h and evaporated to dryness. The residue was washed twice with MeOH, dissolved in 2 mL of DMF and filtered. Et_2O was allowed to diffuse into the filtrate overnight at RT to yield a light brown crystalline solid (55 mg).

General Physical Methods. Elemental analysis was performed using a Perkin-Elmer 2400 series II CHNS analyzer. Cyclic voltammetry study of **1**$(BF_4)_2$ (10^{-3} M) in DMF were performed using a CHI620E electrochemical analyzer (CH Instruments, USA). A three-electrode setup was employed comprised of a glassy carbon working electrode, a platinum wire auxiliary electrode, and a silver wire as the pseudoreference electrode. Tetra-n-butylammonium hexafluorophosphate (0.1 M) was used as the supporting electrolyte. Electrochemical potentials are referenced internally to the ferrocenium/ferrocene couple at 0.0 V. Electronic absorption spectra were recorded using a Cary 60 UV-Vis spectrophotometer. IR spectra of the solid samples as KBr pellets were recorded using a Perkin Elmer Spectrum BX FT-IR. The solution FT-IR data were measured on a Perkin Elmer FT-IR spectrometer (Frontier) instrument. The Mössbauer spectrum was recorded using an alternating constant *WissEl* Mössbauer spectrometer, consisting of an MR 360 Drive Unit, an MV-1000 velocity transducer, and an LND 45431 proportional counter mounted on an LINOS precision bench. The system was operated in a horizontal transmission geometry with source, absorber, and detector in a linear arrangement. The temperature was controlled and maintained using a Janis SHI closed-cycle helium cryostat. Measurements were performed at 80 K. Data acquisition was performed using a 512 channel analyzer. Isomer shifts were referenced versus α-iron metal foil at ambient temperatures. Simulation of experimental data was performed using the *Mfit* program. Magnetic susceptibility measurement of **1**$(BF_4)_2$ was conducted on a Quantum-Design MPMS XL-5 SQUID magnetometer, equipped with a 5 T magnet. The polycrystalline sample was contained in a gel bucket, covered with a drop of low viscosity

perfluoropolyether based inert oil Fomblin Y45 to fix the crystals, and fixed in a non-magnetic sample holder. The maximum measuring temperature of 210 K was chosen because of the pour point of the oil, in order to keep the oil in the frozen state and to avoid the orientation of the crystals parallel to the magnetic field. Each raw data file for the measured magnetic moment was corrected for the diamagnetic contribution of the gel bucket and of the inert oil. The raw data were corrected for the diamagnetic contribution of the compound using $\chi_M^{dia}(\text{sample}) = -0.5 \cdot M \cdot 10^{-6}$ $cm^3 \cdot mol^{-1}$. The data were fit with the *julX* program[53] using the appropriate Heisenberg-Dirac-van-Vleck (HDvV) spin Hamiltonian for isotropic exchange coupling and Zeeman splitting, equation (1).

$$\hat{H} = -2J\hat{S}_1\hat{S}_2 + g\mu_B\vec{B}(\vec{S}_1 + \vec{S}_2) \quad (1)$$

A Curie-behaved paramagnetic impurity (PI) with spin S = 5/2 was included in the fit, according to $\chi(\text{calc}) = (1 - \text{PI}) \cdot \chi + \text{PI} \cdot \chi(\text{mono})$.

EPR spectra were recorded using a Bruker X-band EMX spectrometer equipped with an Oxford liquid helium cryostat. Spectra were recorded on ~2mM frozen solutions using 20 mW microwave power and 100 kHz field modulation at a 1 G amplitude. IR spectroelectrochemistry experiments were performed using a LabOmak UF-SEC thin layer cell, with Pt mesh working and counter electrodes, and an Ag wire pseudoreference electrode. The X-ray photoelectron spectroscopy (XPS) measurement was performed using a focused monochromatized Al−Kα X-ray source (1486.8 eV) in the XPS instrument (Omicron Nano Technology 0571), after etching the sample surface by Ar ion sputtering. The peak fitting was done using Peak Fit Version 4.12 using the Gaussian Deconvolution Method.

N_2O yield Calculation. Compound **1**$(BF_4)_2$ (about 5 μM) was dissolved in 2mL of CH_2Cl_2 in a septum-sealed 25mL round bottom flask with a 14/20 joint. 0.5, 1, or 2 equivalents of $CoCp_2$ (with respect to the concentration of **2**) were dissolved in 0.5 mL of CH_2Cl_2 and syringed into the flask. The

solution was stirred for exactly 5 min prior to evacuating the headspace of the flask via cannula transfer to an evacuated Pike HT gas-IR cell (190 milli-torr) for exactly 20 s. After subtraction of a CH_2Cl_2 blank taken under the exact same conditions, the IR spectrum was converted to absorbance and the N-N stretch of N_2O was integrated using a straight-line baseline correction from 2150 - 2275cm^{-1}. The integration was then compared to a standard curve.[54]

X-ray Structure Determination. The molecular structures of **1**$(BF_4)_2$, **1**$(ClO_4)_2$ and **1**$(OTf)_2$ were determined by single-crystal X-ray structure determinations. Diffraction-quality crystals were obtained as described in the synthesis of the respective compound. Single crystals were coated with Parabar oil and were mounted under a 100 K nitrogen cold stream. Data collections were performed on a Bruker D8VENTURE Micro-focus diffractometer equipped with PHOTON II Detector, with Mo Kα radiation (λ = 0.71073 Å), controlled by the APEX3 (v2017.3-0) software package. The raw data were integrated and corrected for Lorentz and polarization effects with the aid of the Bruker APEX II program suite.[55] Absorption corrections were performed by using SADABS. Space groups were assigned by systematic absences (determined by XPREP) and analysis of metric symmetry and were further checked by PLATON[56, 57] for additional symmetry. Structures were solved by direct methods and refined against all data in the reported 2θ ranges by full-matrix least squares on F2 using the SHELXL program suite[58] in the OLEX 2[59] interface. Hydrogen atoms at idealized positions were included in final refinements. The OLEX 2 interface was used for structure visualization as well as for drawing ORTEP[60, 61] plots. Crystallographic data and final agreement factors are provided in Table S1. The individual CIFs include the refinement details and explanations (wherever applicable). CCDC entries 2035675-2035677 contain the supplementary crystallographic data for this paper. These data are provided free of charge by The Cambridge Crystallographic Data Centre.

Computational Methods. Optimization and frequency calculations on complex **1** were performed with Gaussian 09[62] using the B3LYP functional[63, 64] and 6-311G(d) basis set.[65-67] Complex **1** contains two antiferromagnetically coupled iron centers that were treated by generating four fragments, one fragment containing the *N*-Et-HPTB^{-} ligand scaffold, one containing the hydrosulfide (SH^{-}) ligand and the other two fragments containing one each of the FeNO units. An initial guess calculation was performed first in Gaussian 09 by making one of the Fe-containing fragments anti-ferromagnetically coupled to the other one. This guess was then utilized to begin single-point and geometry-optimization calculations. Once optimized, a frequency calculation was performed, and the final optimized structure was used in a subsequent Orca 4.0.1.2.[68] single point calculation to analyze the electronic structure and calculate Mössbauer parameters. This single point calculation was performed on the Gaussian 09 B3LYP optimized structure (without fragments) utilizing the B3LYP/G functional and 6- 311G(d) basis set with the def2/J auxiliary basis set.[69] The ferromagnetic single point was calculated first, and the spins at one of the FeNO units were then flipped using the Spin Flip operation in Orca.

RESULTS AND DISCUSSION

Synthesis and Characterization. Treatment of a diiron(II)-hydrosulfide compound, [Fe_2(*N*-Et-HPTB)(SH)(H_2O)](BF_4)$_2$ (**2**(BF_4)$_2$),[47] with either excess Ph_3CSNO or with excess NO gas yielded **1**(BF_4)$_2$ in 81% and 85% yields, respectively. The molecular structure of complex **1** revealed an unsymmetrical diiron(II) unit (Figure 1) where one iron center contains the hydrosulfide and one NO, while the other iron center contains one NO and one DMF molecule. Reactivity of coordinated thiolates and NO are quite well known in the literature,[31, 70, 71] although there are few reports for the coexistence of thiolates and NO in the same complex as well.[72-75] On the other hand, NO is known to be highly reactive towards H_2S,[23, 24] and to the best of our knowledge, there are no reports in the literature for the coexistence of NO and hydrosulfide in any nonheme dinuclear complex. It was anticipated that the

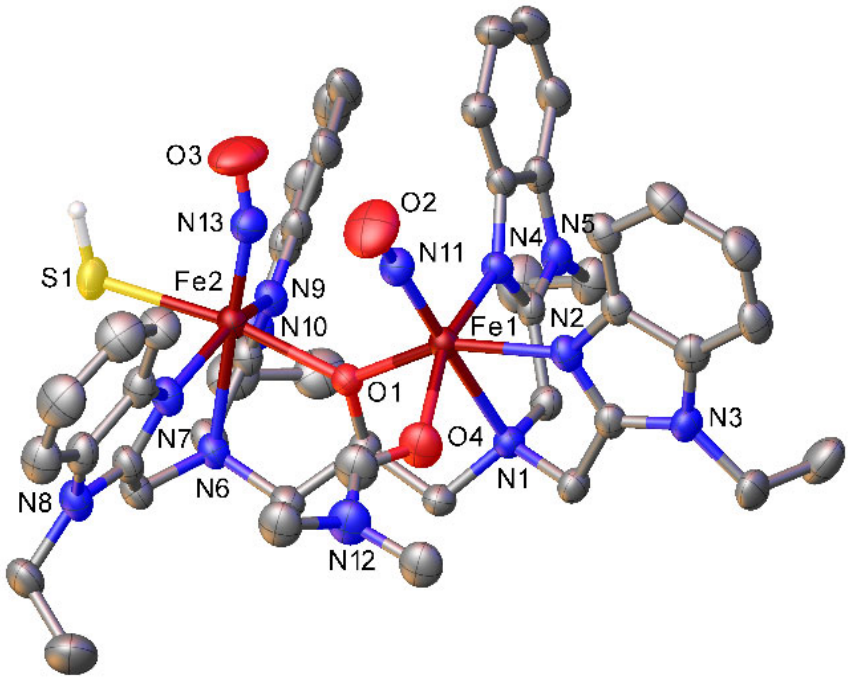

Figure 1. Molecular structure of complex **1** with 30% probability thermal ellipsoids and partial atom labeling scheme. H atoms are omitted (except -SH) for clarity.

incoming NO may react with the coordinated hydrosulfide to generate functionalities like HSNO in a diiron(II) platform. However, in contrast to the expectation based on the high reactivity of NO and H_2S, the coordinated hydrosulfide ligand in **2** did not react with the incoming NO gas, and moreover, NO and hydrosulfide coexist in **1** (Figure 1).

These results prompted us to check the possible reactivity of the coordinated hydrosulfide in **2** and **1** with NO^+ (Scheme 1). Treatment of **2** with 2.5 equivalents of $(NO)(BF_4)$ (reduction potential = 0.87 V and 1 V vs. Cp_2Fe^+/Cp_2Fe in MeCN and CH_2Cl_2, respectively) led to the formation of the mixed-valent diiron(II, III)-SH complex, $[Fe_2(N\text{-Et-HPTB})(SH)(H_2O)(DMF)_2]^{3+}$ (**5**) in 77% yield. Synthesis (via treatment of **2** with $(Cp_2Fe)(BF_4)$) and characterization of **5** has previously been reported by us.[47] Moreover, treatment of **1** (diNOSH complex) with 1.5 equivalents of $(NO)(BF_4)$ again yielded **5** in 81% yield. Reduction of **5** using 1.5 equivalents of Cp_2Co yielded back **2** in 68% yield. Formation of **5** in the

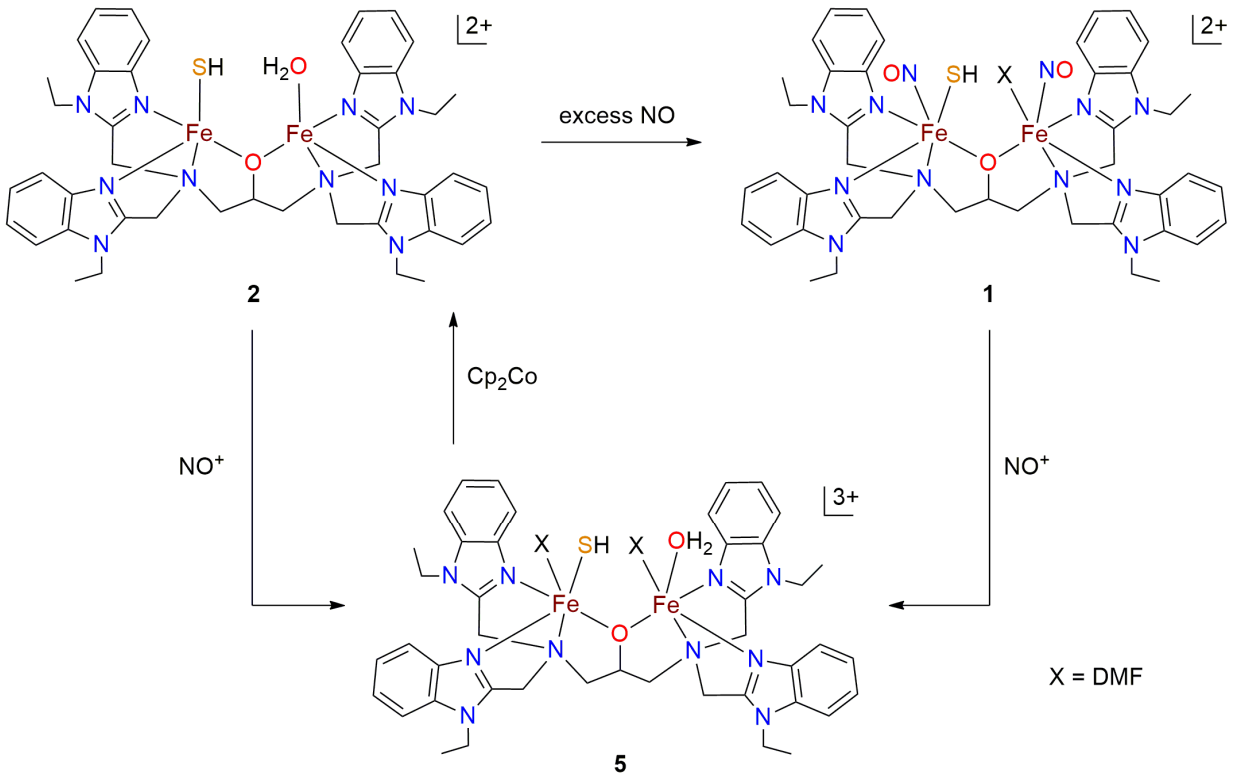

Scheme 1. Reaction of **1** and **2** with NO^+.

above-mentioned reactions has been confirmed by single crystal X-ray structure determination, IR spectroscopy, mass spectrometry and cyclic voltammetry. These results clearly indicate that the coordinated -SH does not react even with NO^+. Furthermore, **1** was subjected to base titration study which was monitored by IR spectroscopy (Figure S1) in order to check whether deprotonation of the coordinated -SH may trigger the reaction with NO. No such reaction, however, could be observed.

The Fe2-SH distance of 2.456(2) Å in **1** is longer than those reported for **2** (2.344(4) Å)[47] and another diiron(II)-bis(hydrosulfide) compound (2.383(1), 2.377(1) Å).[48] The Fe-NO distances of1.761(5) Å (Fe1-N11) and 1.751(5) Å (Fe2-N13), N-O distances of 1.106(6) Å (N11-O2) and 1.150(6) Å (N13- O3) and Fe-N-O angles of 166.9(5)° (Fe1-N11-O2) and 160.3(5)° (Fe2-N13-O3) in

Table 1. Selected bond distances, angles and IR stretching frequencies for **1**$(BF_4)_2$, **1**$(ClO_4)_2$, **1**$(OTf)_2$ and related compounds from literature.

compounds	Fe–N_{NO} (Å)	N-O (Å)	Fe-SH (Å)	Fe-O_{DMF} (Å)	Fe---Fe separation (Å)	<Fe-N-O (°)	<Fe1-O1-Fe2 (°)	ν_{NO} (cm^{-1}) (as KBr pellet)	ν_{SH} (cm^{-1}) (as KBr pellet)
1$(BF_4)_2$	1.761(5) 1.751(5)	1.106(6) 1.150(6)	2.456(2)	2.146(4)	3.749	166.9(5) 160.3(5)	132.4(2)	1785	2516
1$(ClO_4)_2$	1.759(3) 1.761(4)	1.159(5) 1.152(5)	2.406(1)	2.153(3)	3.625	167.4(4) 157.0(4)	127.9(2)	1782	2509
1$(OTf)_2$	1.758(5) 1.853(6)	1.127(6) 0.973(6)	2.435(2)	2.095(4)	3.679	165.2(5) 157.6(7)	129.9(2)	1782	2532
2$(BF_4)_2)$[47]	-----	-----	2.344(4)	-----	3.677	-----	132.1(3)	-----	2515
3$(BF_4)_3$[31]	1.729(7) 1.748(7)	1.123(8) 1.147(8)	-----	2.073(6) 2.153(6)	3.669	174.9(8) 164.9(7)	131.1(2)	1782	-----
4$(BF_4)_3$[30]	1.775(5)	1.066(7)	-----	2.159(4) 2.339(5) 2.082(4)	3.605	160.5(7)	129.6(2)	1768	-----

1 are comparable with those reported for the FNOR model compound, [Fe_2(*N*-Et-HPTB)$(NO)_2(DMF)_2$]$(BF_4)_3$ (**3**$(BF_4)_3$),[31] and its mononitrosyl analogue, [Fe_2(*N*-Et-HPTB)$(NO)(DMF)_3$]$(BF_4)_3$ (**4**$(BF_4)_3$),[30] (Table 1) and other nitrosylated diiron compounds.[26, 29, 76] The metric parameters of **1**$(ClO_4)_2$ and **1**$(OTf)_2$ (Figure S2) are similar with those obtained for **1**$(BF_4)_2$ (Table 1). The presence of a coordinated hydrosulfide in **1** was confirmed by the appearance of ν_{SH} at 2516 cm^{-1} (Figure S3) which is nearly identical to that reported for **2** (2515 cm^{-1}),[47] and for another diiron(II)-hydrosulfide compound.[48] The presence of sulfur in **1** was further confirmed by X-ray photoelectron spectroscopy (XPS) of **1**$(BF_4)_2$, which showed the characteristic peak for sulfur (S 2p)[47, 48] at 162.0 eV (Figure 2b). The ν_{NO} value of 1785 cm^{-1} (as KBR pellet, Figure S3; 1796 cm^{-1} in MeCN, Figure S4) for **1**$(BF_4)_2$ falls within the range of 1720−1840 cm^{-1} typically observed for high- spin (hs) non-heme $\{FeNO\}^7$ complexes.[26, 27, 29-31, 76-78] The amide vibration from the metal-coordinated DMF is observed at 1654 cm^{-1} (as KBR pellet), while the solution IR spectrum shows the vibrations from metal-

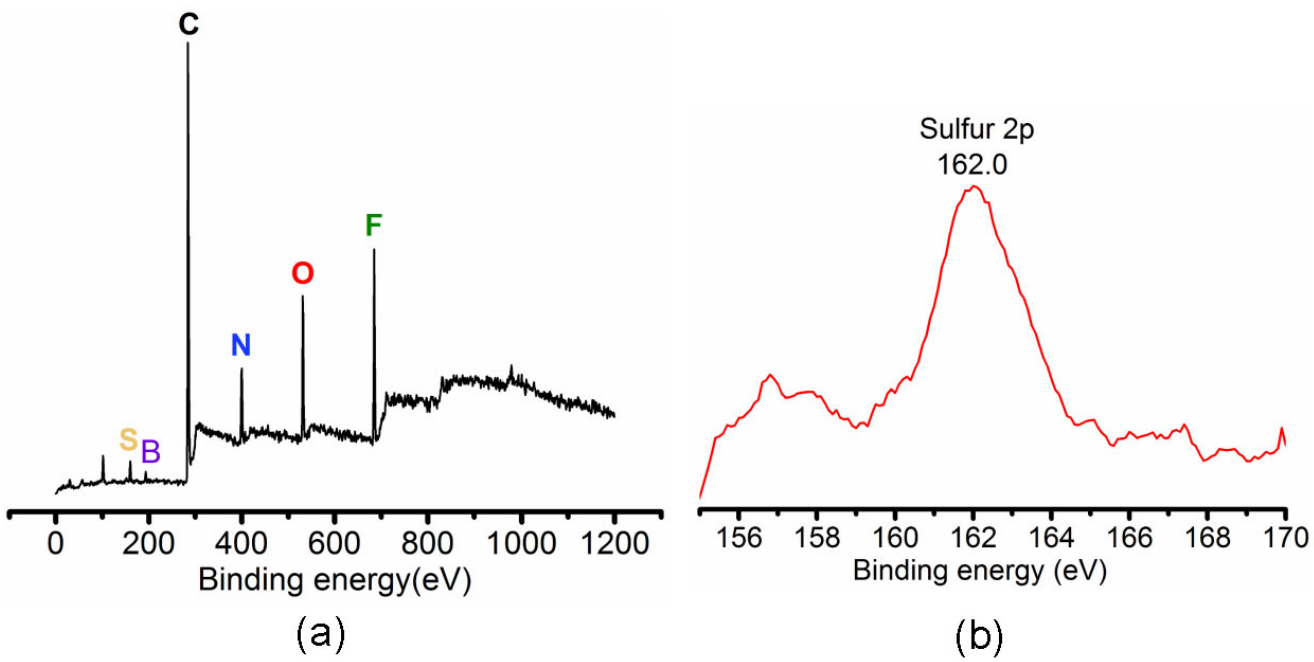

Figure 2. X-ray photoelectron spectra for **1**$(BF_4)_2$: (a) full range, (b) S 2p.

coordinated DMF and free DMF at 1654 and 1670 cm^{-1}, respectively, which is consistent with literature reports.[28, 30, 31] The electronic absorption spectrum of **1**$(BF_4)_2$ (Figure S5) shows three distinct transitions and is in agreement with data for other non-heme hs-{FeNO}^{7} complexes.[9, 30, 31, 76] The broad features observed at 600 nm ($\varepsilon = 210 \pm 5$ M^{-1} cm^{-1}) and 525 nm ($\varepsilon = 245 \pm 35$ M^{-1} cm^{-1}) are attributed to mixed d-d and $NO^-(\pi^*)$ to Fe^{III} charge transfer transition.[9, 79] Compound **1**$(BF_4)_2$ exhibits an additional shoulder at 425 nm ($\varepsilon = 518 \pm 75$ M^{-1} cm^{-1}), which sits on the tail of the strong UV band at 342 nm (3450 ± 40). Mass spectrometry of **1** (in MeCN in the presence of NO, see Figure S6) showed the molecular ion peak at m/z = 464.1357 for $[Fe_2(N\text{-Et-HPTB})(SH)(NO)_2]^{2+}$ (calcd m/z = 464.1347). Despite the different ligation of the two iron centers, the ^{57}Fe Mössbauer spectrum of **1**$(BF_4)_2$ (Figure 3) features only one quadrupole doublet with an isomer shift, $\delta = 0.65$ mm/s. Very similar isomer shifts have been reported for **3** (0.64 mm/s)[31] and other complexes which feature one or more hs-{FeNO}^{7} units.[27, 29-31, 76, 77] Similar to **3**,[31] complex **1** was also found to be EPR silent. A superconducting quantum interference device (SQUID) magnetometry measurement of solid **1**$(BF_4)_2$ revealed significant

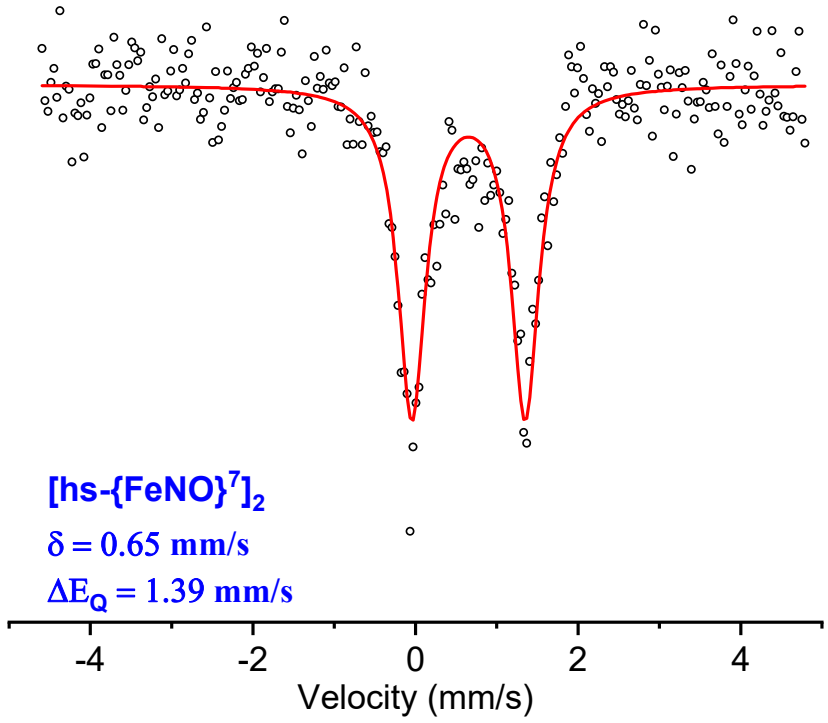

Figure 3. ^{57}Fe Mössbauer spectrum of a polycrystalline sample of **1**$(BF_4)_2$ at 80K.

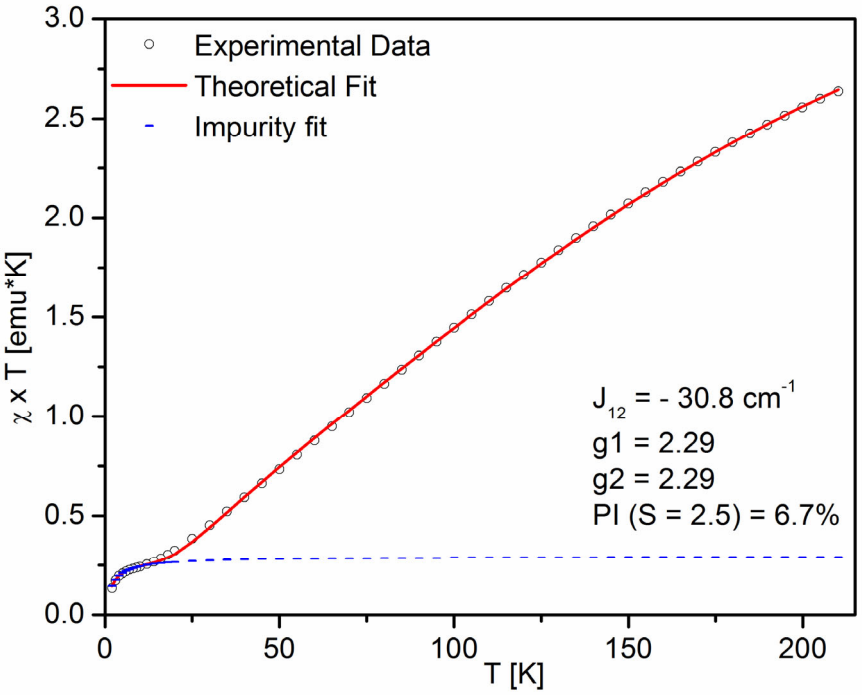

Figure 4. SQUID magnetometry measurements of **1**$(BF_4)_2$. The solid red line represents the best fit using S1 = S2 = 3/2 for **1** and the indicated parameters.

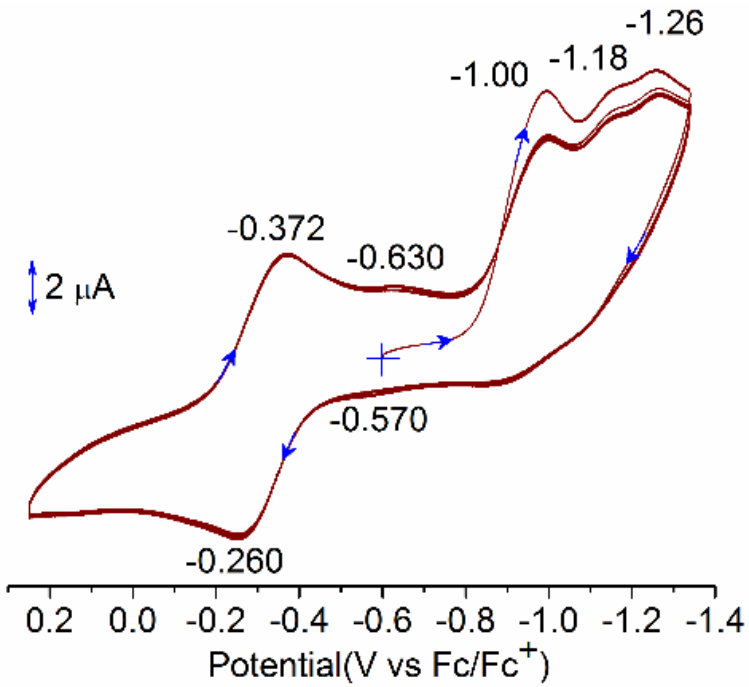

Figure 5. Cyclic voltammetric trace (multiple scans) for **1**$(BF_4)_2$ in DMF.

antiferromagnetic coupling with $J = -30.8$ cm^{-1} between the two hs-{FeNO}^{7} units (Figure 4), which is very similar to that observed previously (-28.3 cm^{-1}) for **3**.[31] This result reflects the Fe^{III}–NO^- electronic structure of the two hs-{FeNO}^{7} units.[31] Together, the molecular structure determination, elemental analysis, mass spectrometry, SQUID magnetometry, electronic absorption, IR, Mössbauer, EPR and X-ray photoelectron spectroscopic measurements thus confirm the formulation of **1** as a [(HS)hs-{FeNO}^{7}/hs-{FeNO}^{7}] species. The complexes **1**-**3** and the dinucleating ligand, H*N*-ET-HPTB are shown in Scheme 2.

A cyclic voltammetry study of **1** showed three irreversible reduction processes at –1.0, –1.18 and –1.26 V (Figure 5). In comparison, **3** showed two irreversible reduction processes at −1.18 and −1.30 V,[31] while its mononitrosyl analogue, **4**$(BF_4)_3$,[30] showed only one irreversible reduction at −1.02 V under identical conditions.[30] We therefore propose that the three reduction events for **1** arise due to the

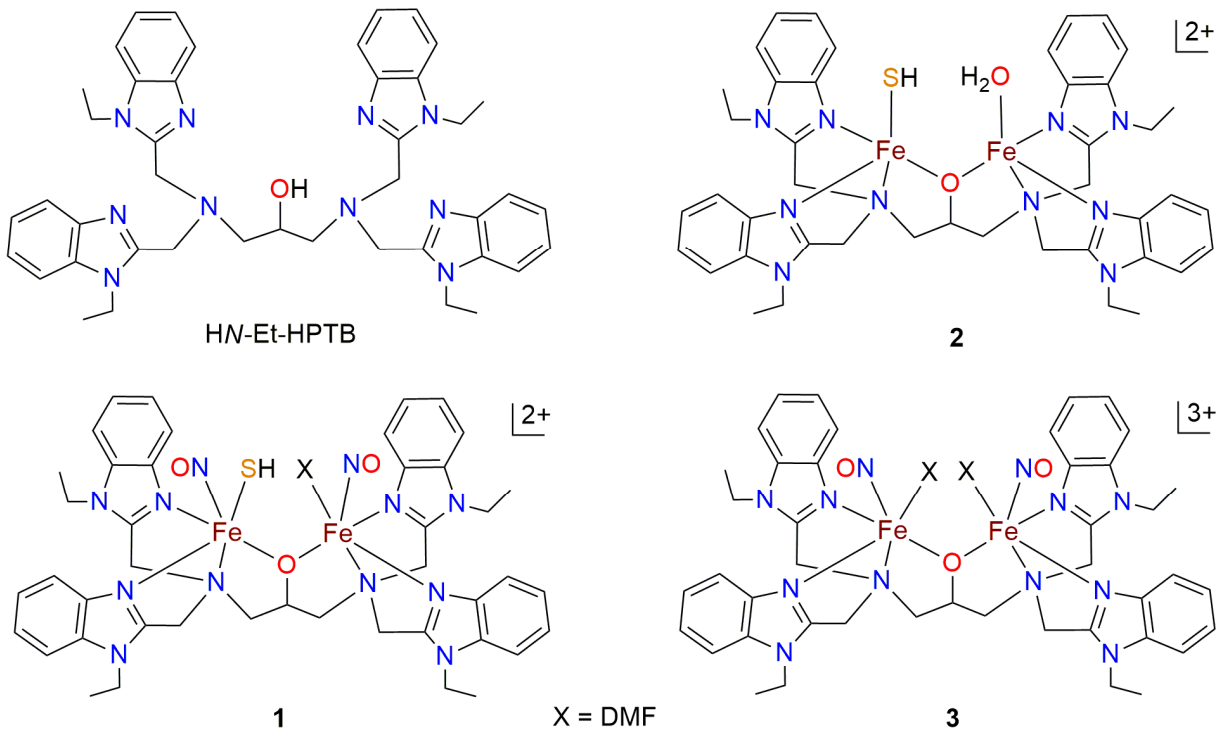

Scheme 2. Complexes **1**-**3** and the dinucleating ligand, H*N*-ET-HPTB

partial dissociation of one NO to generate some amount of a mononitrosylated species under electrochemical conditions in solution. This result suggests that the NO ligands in **1** are labile. The new redox couple generated in the return scan at $E_{pa} = -0.570$ ($E_{pc} = -0.630$) for **1** may be attributed[31] to an Fe^{II}-O-Fe^{II}/Fe^{II}-OH-Fe^{II} species, formed from the reduction of the initial reaction product, a mixed-valent Fe^{II}-O-Fe^{III} species, generated after release of N_2O from reduced **1**.

Generation of N_2O by Complex 1. Considering the similarity in the structural parameters and spectroscopic properties of **1** with the FNOR functional model complex **3**,[31] N_2O production activity of **1** was examined. Complex **1** does not produce N_2O in solution in the absence of a reductant (Figure S4), similar to **3** and other previously reported dinitrosyl diiron complexes[26, 28, 76] and the dinitrosyl adducts of ribonucleotide reductase and methane monoxygenase.[9] However, **1** generates N_2O upon chemical (by cobaltocene) and electrochemical reduction at room temperature. The latter was examined by IR

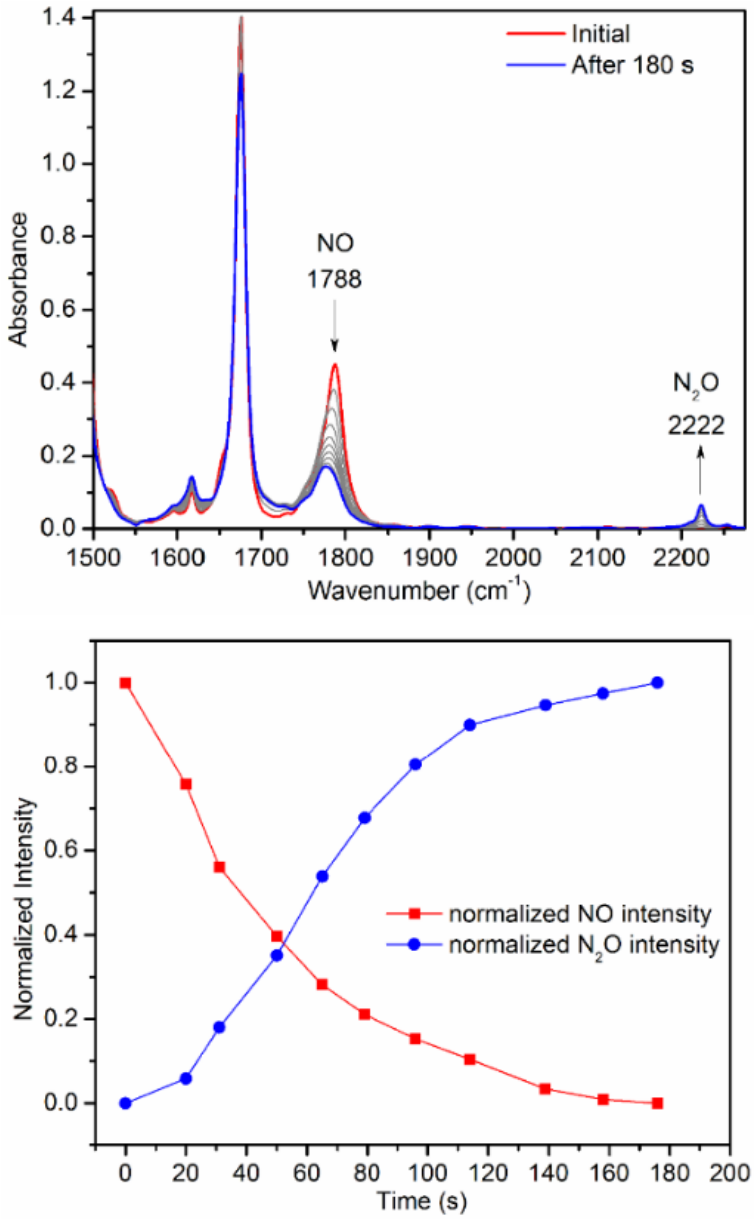

Figure 6. Generation of N_2O upon electrochemical reduction of **1**$(BF_4)_2$. Experimental Conditions: [**1**$(BF_4)_2$] = 11.6 mM in CH_2Cl_2; hold potential = -1.5 V vs. Ag wire; 0.1 mM $(Et_4N)(BF_4)$.

spectro-electrochemistry (Figure 6), which confirmed the formation of N_2O from **1** without any detectable intermediates. Rapid production of N_2O upon reduction of **1** by 2 equiv of cobaltocene was also confirmed by IR spectroscopic analysis of the reaction headspace. Integration of the N-N stretching band of N_2O against a calibration curve revealed ~91% yield of N_2O (based on the concentration of

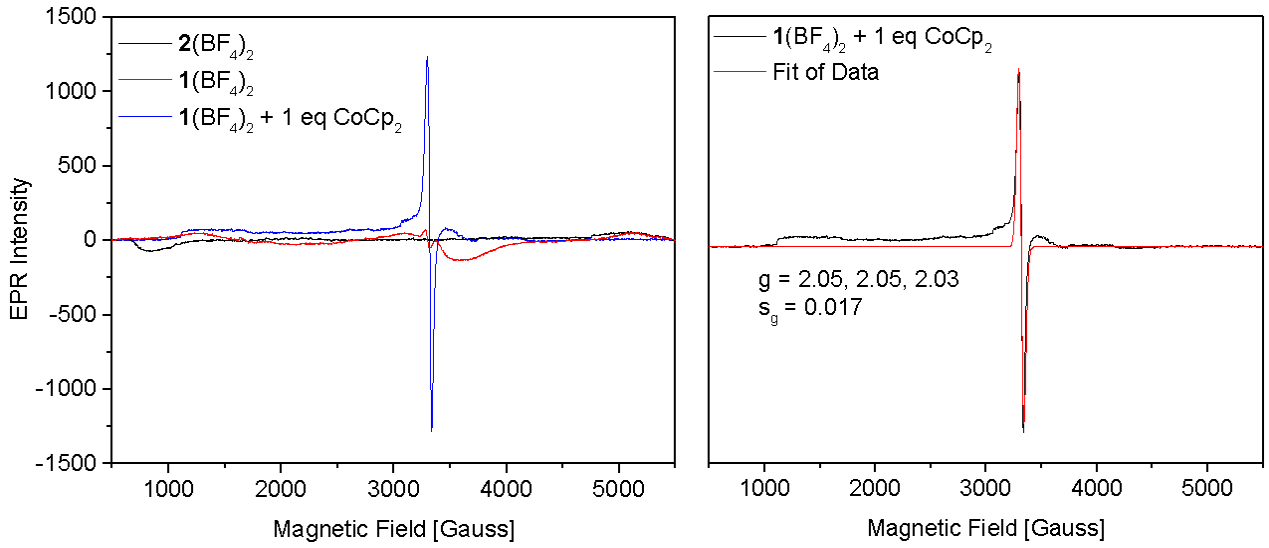

Figure 7. Left. EPR spectra of **1**$(BF_4)_2$ and **2**$(BF_4)_2$ in MeCN demonstrate that both of the compounds are initially EPR silent. Upon one-electron reduction of **1**at RT in CH_2Cl_2, a S = ½ signal arises. EPR conditions: [**1**$(BF_4)_2$] = ~2 mM, [**2**$(BF_4)_2$] = 2 mM, 9.336 GHz microwave frequency, 20 mW microwave power, 1 G modulation amplitude and 10.24 ms time constant. EPR data were recorded at 4 K. Right. Spin Count simulation of the EPR spectrum resulting from the reduction of **1** with 1 eq $CoCp_2$ (taken in CH_2Cl_2). Simulation parameters: $g_x = g_y = 2.05$, $g_z = 2.03$; $s_{g(x,y,z)} = 0.017$.

1$(BF_4)_2$) within 5 minutes of cobaltocene addition (Figure S10). Furthermore, it was observed that even 1 equiv of cobaltocene was sufficient for the production of N_2O from **1** with 84% yield. Thus, **1** is following a semireduced mechanism for the production of N_2O. A semireduced mechanism was previously reported[27] by two of us (N.L. and F.M.) for a dinitrosyl diiron compound, where it was shown that this mechanism constitutes an efficient pathway for the reduction of NO to N_2O by model systems, and potentially by FNORs as well. Recently, we have shown that **3** also follows a semireduced pathway for the reduction of NO to N_2O and that a broad S = 1/2 EPR signal ($\langle g \rangle$ = 1.55, 1.79, 2.03) is generated due to the formation of a mixed-valent diiron(II, III) species upon one-electron reduction of **3**.[31] In line with these results, a mixture of **1** and 1 equiv of cobaltocene indeed generated an S = 1/2

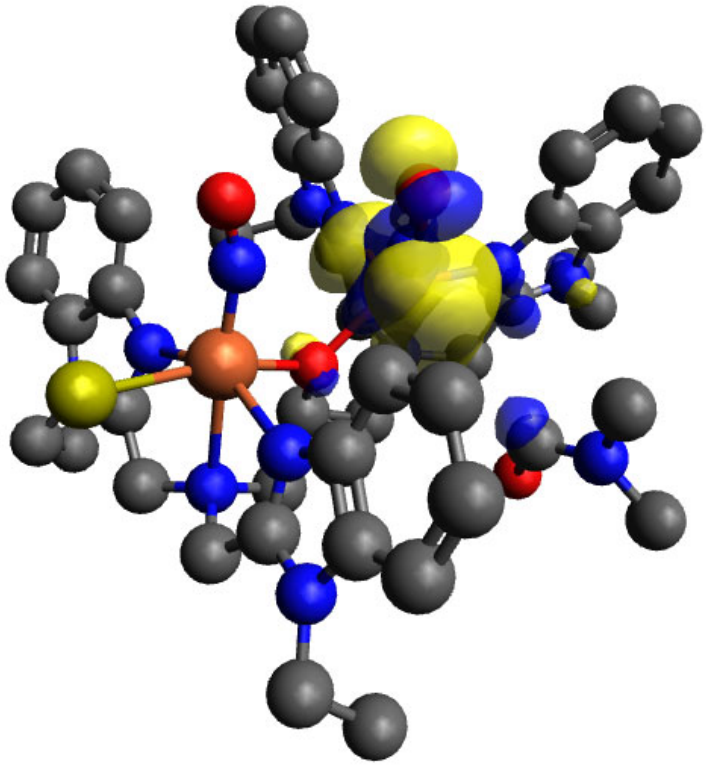

Figure 8. Contour plot of the Fe-NO antibonding $d_{yz}\_\pi^*_y$ orbital that is occupied upon one-electron reduction of **1** to the hs-{FeNO}^{7}(SH)/hs-{FeNO}^{8}(DMF) state.

EPR signal ($\langle g \rangle$ = 2.05, 2.05, 2.03; Figure 7, see also Figure S15 for EPR simulation of the mixed-valent reduction product) and thus further confirmed the semireduced mechanism for the reduction of NO to N_2O by **1**. The semireduced mechanism is also supported by the mass spectrometric study of a reaction mixture involving **1** and 1 equiv of cobaltocene, which indicated the formation of a mixed-valent diiron(II, III) species, $[Fe_2(N\text{-Et-HPTB})(\mu\text{-O})]^{2+}$, along with its hydroxo bridged dimer, $[Fe_4(N\text{-Et-HPTB})_2(\mu\text{-OH})_4]^{4+}$ (Figures S11-S12). On the other hand, a reaction mixture involving **1** and 2 equiv of cobaltocene indicated the formation of all-ferrous tetrameric species, $[Fe_4(N\text{-Et-HPTB})_2(\mu\text{-OH})_2(H_2O)_2]^{4+}$ and $[Fe_4(N\text{-Et-HPTB})_2(\mu\text{-OH})_2]^{4+}$ (Figures S13-S14). These results further indicate that the coordinated hydrosulfide is likely lost after N_2O formation.

Theoretical Calculation. Due to the asymmetric nature of **1** (Figure 1), density functional theory (DFT) was employed to evaluate the electronic structure of its one-electron reduced form and the site of

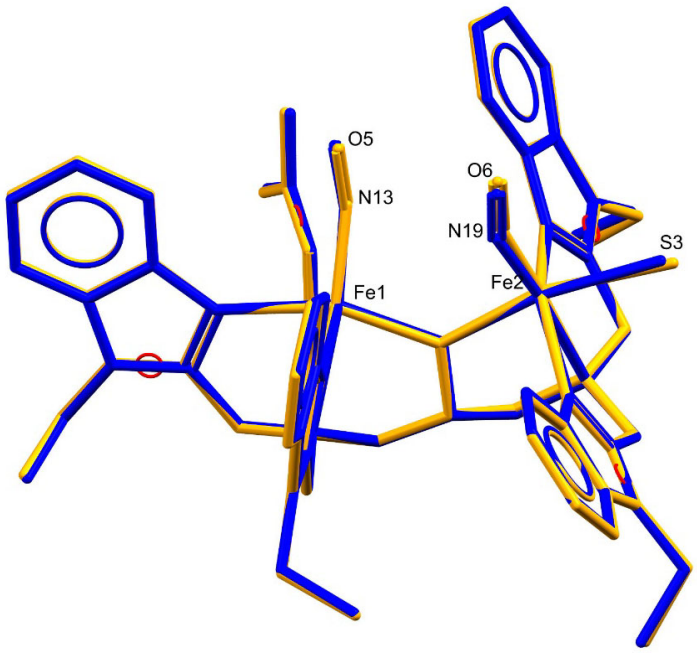

Figure 9. Overlay of the two hs-{FeNO}^{7}(SH)/{FeNO}^{8}(DMF) structures generated from geometry optimizations on initial hs-{FeNO}^{7}(SH)/{FeNO}^{8}(DMF) and hs-{FeNO}^{8}(SH)/{FeNO}^{7}(DMF) states. It is evident from the figure that the main structural difference lies in the Fe-SH distance.

reduction. The B3LYP/6-311(G)d optimized structure of **1** shows Fe-NO bond lengths of 1.752 Å and 1.761 Å at the hs-{FeNO}^{7}(SH) and hs-{FeNO}^{7}(DMF) sites, respectively, and Fe-N-O bond angles of 160.3° and 166.9° (Table S2). These values are all typical for hs-{FeNO}^{7} complexes[9] and are in good agreement with the structural parameters from the crystal structure of **1** (see Tables 1 and S2). The B3LYP calculations for **1** overestimate the frequencies of each N-O stretch, predicting values of 1811 and 1861 cm^{-1} for the hs-{FeNO}^{7}(SH) and hs-{FeNO}^{7}(DMF) units, respectively, which is common when using hybrid functionals like B3LYP.[80]

The one-electron reduction to the hs-{FeNO}^{7}(SH)/hs-{FeNO}^{8}(DMF) state leads to an elongation of the Fe-NO and N-O bond lengths at the hs-{FeNO}^{8}(DMF) center from 1.793 and 1.164 Å to 1.806 Å and 1.207 Å, respectively (Table S3). The Fe-N-O bond angle becomes more bent at 149.8° and the

N-O stretching frequency significantly decreases to 1671 cm^{-1}. It is important to note that in the gas-phase DFT-optimized structure of the hs-{FeNO}^{7}(SH)/hs-{FeNO}^{8}(DMF) state, the DMF ligand twists such that the DMF does not coordinate the Fe-center, but instead provides a moderately strong H-bonding interaction to the NO (H-N distance = 2.90 Å). In solution, the reduced Fe-center likely loses the DMF ligand to the bulk solvent. Single point calculations on the optimized structure show that the additional electron occupies the d_{yz}_π^*_y orbital (Figure 8), which is antibonding with respect to the Fe-NO bond. In line with this, the spin density at the hs-{FeNO}^{8}(DMF) unit increases (Table S4), suggesting a decreased covalency in the Fe-NO bond. This finding is also in agreement with the predicted, dramatic drop in the N-O stretch of the hs-{FeNO}^{8}(DMF) center. The occupation of the antibonding d_{yz}_π^*_y orbital leads to a strong activation of the corresponding hs-{FeNO}^{8} unit, as previously discussed.[80]

Interestingly, the geometry optimizations of the hs-{FeNO}^{7}(SH)/hs-{FeNO}^{8}(DMF) and hs-{FeNO}^{8}(SH)/hs-{FeNO}^{7}(DMF) states ultimately converged to two slightly different hs-{FeNO}^{7}(SH)/hs-{FeNO}^{8}(DMF) structures (overlaid in Figure 9 and structural parameters are compared in Table S3). The structure resulting from the hs-{FeNO}^{7}(SH)/hs-{FeNO}^{8}(DMF) starting point is 5.3 kcal/mol lower in energy than the structure resulting from the hs-{FeNO}^{8}(SH)/hs-{FeNO}^{7}(DMF) starting point. In both cases, Orca single point calculations on the optimized structures show that the antibonding d_{yz}_π^*_y orbital of the hs-{FeNO}^{8}(DMF) center is occupied upon one-electron reduction.

CONCLUSION

In summary, an unprecedented monohydrosulfido dinitrosyl diiron compound (**1**$(BF_4)_2$) has been synthesized and extensively characterized. Complex **1** features a [(HS)hs-{FeNO}^{7}/hs-{FeNO}^{7}]

formulation and produces N_2O in high yield following a semireduced mechanism, where one-electron reduction generates a reactive hs-{FeNO}^{8} center via occupation of an Fe-NO antibonding orbital. Isolation of **1** confirms that in stark contrast to the known reactivity of H_2S and NO,[23, 24] the iron-bound hydrosulfide in **1** does not react with NO. Interestingly, the coordinated hydrosulfide in **1** and **2** does not even react with NO^+ either. Despite of featuring a unique molecular structure, the structural parameters and the spectroscopic properties of the FeNO units as well as the N_2O production activity of **1** are quite similar to that observed for the previously reported functional model complex of FNORs, **3**.[31] These results thus strongly indicate that the coordinated hydrosulfide is acting as a spectator ligand during the generation of N_2O by **1**.

ASSOCIATED CONTENT

Supporting Information. The Supporting Information is available free of charge on the ACS Publications website.

Experimental procedure, spectroscopic data and N_2O yield calculation (PDF).

X-ray crystallographic data (cif) for **1**$(BF_4)_2$, **1**$(ClO_4)_2$ and **1**$(OTf)_2$.

AUTHOR INFORMATION

Corresponding Author

*Email: lehnertn@umich.edu; icam@iacs.res.in

Author Contributions

The manuscript was written through contributions of all authors. All authors have given approval to the final version of the manuscript.

Notes

The authors declare no competing financial interest.

ACKNOWLEDGMENT

This work was supported by SERB, India (EMR/2017/000828 to A.M.) and CSIR India (01(2972)/19/EMR-II to A.M.) and by the National Science Foundation (CHE-2002855 to NL). N.P. acknowledge CSIR, India, for SRF. F.M. acknowledges support from the Georg-August-University Göttingen.

References.

1. Moncada, S.; Higgs, E. A. The discovery of nitric oxide and its role in vascular biology. *Brit. J. Pharmacol.* **2006**, *147*, S193-S201.
2. Culotta, E.; Koshland, D. E. NO NEWS IS GOOD-NEWS. *Science* **1992**, *258*, 1862-1865
3. Moncada, S.; Palmer, R. M.; Higgs, E. A. Nitric oxide: physiology, pathophysiology, and pharmacology. *Pharmacol. Rev.* **1991**, *43*, 109-142.
4. Ignarro, L. *Nitric Oxide: Biology and Pathobiology*. Academic Press: San Diego, 2000.
5. Missall, T. A.; Lodge, J. K.; McEwen, J. E. Mechanisms of Resistance to Oxidative and Nitrosative Stress: Implications for Fungal Survival in Mammalian Hosts. *Eukaryot. Cell* **2004**, *3*, 835-846.
6. MacMicking, J.; Xie, Q. W.; Nathan, C. Nitric oxide and macrophage function. *Annu. Rev. Immunol.* **1997**, *15*, 323-350.
7. Kurtz, D. M., Jr. Flavo-diiron enzymes: nitric oxide or dioxygen reductases? *Dalton Trans.* **2007**, 4115-4121.
8. Khatua, S.; Majumdar, A. Flavodiiron nitric oxide reductases: Recent developments in the mechanistic study and model chemistry for the catalytic reduction of NO. *J. Inorg. Biochem.* **2015**, *142*, 145-153.
9. Berto, T. C.; Speelman, A. L.; Zheng, S.; Lehnert, N. Mono- and dinuclear non-heme iron–nitrosyl complexes: Models for key intermediates in bacterial nitric oxide reductases. *Coord. Chem. Rev.* **2013**, *257*, 244-259.
10. Lehnert, N.; Fujisawa, K.; Camarena, S.; Dong, H. T.; White, C. J. Activation of Non-Heme Iron-Nitrosyl Complexes: Turning Up the Heat. *ACS Catal.* **2019**, *9*, 10499-10518.
11. Gardner, A. M.; Helmick, R. A.; Gardner, P. R. Flavorubredoxin, an Inducible Catalyst for Nitric Oxide Reduction and Detoxification in Escherichia coli. *J. Biol. Chem.* **2002**, *277*, 8172-8177.

12. Hayashi, T.; Caranto, J. D.; Wampler, D. A.; Kurtz, D. M., Jr.; Moënne-Loccoz, P. Insights into the Nitric Oxide Reductase Mechanism of Flavodiiron Proteins from a Flavin-Free Enzyme. *Biochemistry* **2010**, *49*, 7040-7049.
13. Silaghi-Dumitrescu, R.; Kurtz, D. M., Jr.; Ljungdahl, L. G.; Lanzilotta, W. N. X-ray Crystal Structures of Moorella thermoacetica FprA. Novel Diiron Site Structure and Mechanistic Insights into a Scavenging Nitric Oxide Reductase[†,‡]. *Biochemistry* **2005**, *44*, 6492-6501.
14. Blomberg, L. M.; Blomberg, M. A.; Siegbahn, P. M. Theoretical study of the reduction of nitric oxide in an A-type flavoprotein. *J. Biol. Inorg. Chem.* **2007**, *12*, 79-89.
15. Caranto, J. D.; Weitz, A.; Hendrich, M. P.; Kurtz, D. M. The Nitric Oxide Reductase Mechanism of a Flavo-Diiron Protein: Identification of Active-Site Intermediates and Products. *J. Am. Chem. Soc.* **2014**, *136*, 7981-7992.
16. Wang, R. Two's company, three's a crowd: can H2S be the third endogenous gaseous transmitter? *FASEB J.* **2002**, *16*, 1792-1798.
17. Wang, R. Physiological Implications of Hydrogen Sulfide: A Whiff Exploration That Blossomed. *Physiol. Rev.* **2012**, *92*, 791-896.
18. Liu, Y.-H.; Lu, M.; Hu, L.-F.; Wong, P. T.-H.; Webb, G. D.; Bian, J.-S. Hydrogen Sulfide in the Mammalian Cardiovascular System. *Antioxid. Redox Sign.* **2012**, *17*, 141-185.
19. Hosoki, R.; Matsuki, N.; Kimura, H. The Possible Role of Hydrogen Sulfide as an Endogenous Smooth Muscle Relaxant in Synergy with Nitric Oxide. *Biochem. Biophys. Res. Commun.* **1997**, *237*, 527-531.
20. Zhao, W.; Zhang, J.; Lu, Y.; Wang, R. The vasorelaxant effect of H_2S as a novel endogenous gaseous K_{ATP} channel opener. *EMBO J.* **2001**, *20*, 6008-6016.
21. Abe, K.; Kimura, H. The possible role of hydrogen sulfide as an endogenous neuromodulator. *J. Neurosci.* **1996**, *16*, 1066-1071.
22. Kimura, H. Hydrogen sulfide as a neuromodulator. *Mol. Neurobiol.* **2002**, *26*, 13-19.
23. Ivanovic-Burmazovic, I.; Filipovic, M. R. Saying NO to H_2S: A Story of HNO, HSNO, and $SSNO^-$. *Inorg. Chem.* **2019**, *58*, 4039-4051.
24. Marcolongo, J. P.; Venâncio, M. F.; Rocha, W. R.; Doctorovich, F.; Olabe, J. A. NO/H_2S "Crosstalk" Reactions. The Role of Thionitrites (SNO^-) and Perthionitrites ($SSNO^-$). *Inorg. Chem.* **2019**, *58*, 14981-14997.
25. Dong, H. T.; White, C. J.; Zhang, B.; Krebs, C.; Lehnert, N. Non-Heme Diiron Model Complexes Can Mediate Direct NO Reduction: Mechanistic Insight into Flavodiiron NO Reductases. *J. Am. Chem. Soc.* **2018**, *140*, 13429-13440.
26. Zheng, S.; Berto, T. C.; Dahl, E. W.; Hoffman, M. B.; Speelman, A. L.; Lehnert, N. The Functional Model Complex $[Fe_2(BPMP)(OPr)(NO)_2](BPh_4)_2$ Provides Insight into the Mechanism of Flavodiiron NO Reductases. *J. Am. Chem. Soc.* **2013**, *135*, 4902-4905.
27. White, C. J.; Speelman, A. L.; Kupper, C.; Demeshko, S.; Meyer, F.; Shanahan, J. P.; Alp, E. E.; Hu, M.; Zhao, J.; Lehnert, N. The Semireduced Mechanism for Nitric Oxide Reduction by Non-Heme Diiron Complexes: Modeling Flavodiiron Nitric Oxide Reductases. *J. Am. Chem. Soc.* **2018**, *140*, 2562-2574.
28. Jiang, Y.; Hayashi, T.; Matsumura, H.; Do, L. H.; Majumdar, A.; Lippard, S. J.; Moënne-Loccoz, P. Light-induced N_2O production from a nonheme iron-nitrosyl dimer. *J. Am. Chem. Soc.* **2014**, *136*, 12524-12527.
29. Kindermann, N.; Schober, A.; Demeshko, S.; Lehnert, N.; Meyer, F. Reductive Transformations of a Pyrazolate-Based Bioinspired Diiron–Dinitrosyl Complex. *Inorg. Chem.* **2016**, *55*, 11538-11550.

30. Jana, M.; Pal, N.; White, C. J.; Kupper, C.; Meyer, F.; Lehnert, N.; Majumdar, A. Functional Mononitrosyl Diiron(II) Complex Mediates the Reduction of NO to N_2O with Relevance for Flavodiiron NO Reductases. *J. Am. Chem. Soc.* **2017**, *139*, 14380-14383.
31. Jana, M.; White, C. J.; Pal, N.; Demeshko, S.; Cordes, C.; Meyer, F.; Lehnert, N.; Majumdar, A. Functional Models for the Mono- and Dinitrosyl Intermediates of FNORs: Semireduction versus Superreduction of NO. *J. Am. Chem. Soc.* **2020**, *142*, 6600-6616.
32. Rock, P. A.; Swinehart, J. H. The Kinetics of the Aqueous Hydrogen Sulfide-Nitroprusside System. *Inorg. Chem.* **1966**, *5*, 1078-1079.
33. Quiroga, S. L.; Almaraz, A. E.; Amorebieta, V. T.; Perissinotti, L. L.; Olabe, J. A. Addition and Redox Reactivity of Hydrogen Sulfides (H_2S/HS^-) with Nitroprusside: New Chemistry of Nitrososulfide Ligands. *Chem. Eur. J.* **2011**, *17*, 4145-4156.
34. Filipovic, M. R.; Ivanovic-Burmazovic, I. The Kinetics and Character of the Intermediates Formed in the Reaction between Sodium Nitroprusside and Hydrogen Sulfide Need Further Clarification. *Chem. Eur. J.* **2012**, *18*, 13538-13540.
35. Filipovic, M. R.; Eberhardt, M.; Prokopovic, V.; Mijuskovic, A.; Orescanin-Dusic, Z.; Reeh, P.; Ivanovic-Burmazovic, I. Beyond H_2S and NO Interplay: Hydrogen Sulfide and Nitroprusside React Directly to Give Nitroxyl (HNO). A New Pharmacological Source of HNO. *J. Med. Chem.* **2013**, *56*, 1499-1508.
36. Fitzpatrick, J.; Kalyvas, H.; Filipovic, M. R.; Ivanović-Burmazović, I.; MacDonald, J. C.; Shearer, J.; Kim, E. Transformation of a Mononitrosyl Iron Complex to a [2Fe-2S] Cluster by a Cysteine Analogue. *J. Am. Chem. Soc.* **2014**, *136*, 7229-7232.
37. Tsai, M.-L.; Tsou, C.-C.; Liaw, W.-F. Dinitrosyl Iron Complexes (DNICs): From Biomimetic Synthesis and Spectroscopic Characterization toward Unveiling the Biological and Catalytic Roles of DNICs. *Acc. Chem. Res.* **2015**, *48*, 1184-1193.
38. Tsai, M.-L.; Chen, C.-C.; Hsu, I. J.; Ke, S.-C.; Hsieh, C.-H.; Chiang, K.-A.; Lee, G.-H.; Wang, Y.; Chen, J.-M.; Lee, J.-F.; Liaw, W.-F. Photochemistry of the Dinitrosyl Iron Complex $[S_5Fe(NO)_2]^-$ Leading to Reversible Formation of $[S_5Fe(\mu\text{-}S)_2FeS_5]^{2-}$: Spectroscopic Characterization of Species Relevant to the Nitric Oxide Modification and Repair of [2Fe−2S] Ferredoxins. *Inorg. Chem.* **2004**, *43*, 5159-5167.
39. Lu, T.-T.; Huang, H.-W.; Liaw, W.-F. Anionic Mixed Thiolate−Sulfide-Bridged Roussin's Red Esters $[(NO)_2Fe(\mu\text{-}SR)(\mu\text{-}S)Fe(NO)_2]^-$ (R = Et, Me, Ph): A Key Intermediate for Transformation of Dinitrosyl Iron Complexes (DNICs) to [2Fe-2S] Clusters. *Inorg. Chem.* **2009**, *48*, 9027-9035.
40. Tsou, C.-C.; Chiu, W.-C.; Ke, C.-H.; Tsai, J.-C.; Wang, Y.-M.; Chiang, M.-H.; Liaw, W.-F. Iron(III) Bound by Hydrosulfide Anion Ligands: NO-Promoted Stabilization of the $[Fe^{III}–SH]$ Motif. *J. Am. Chem. Soc.* **2014**, *136*, 9424-9433.
41. Fitzpatrick, J.; Kim, E. Synthetic Modeling Chemistry of Iron–Sulfur Clusters in Nitric Oxide Signaling. *Acc. Chem. Res.* **2015**, *48*, 2453-2461.
42. Tran, C. T.; Williard, P. G.; Kim, E. Nitric Oxide Reactivity of [2Fe-2S] Clusters Leading to H_2S Generation. *J. Am. Chem. Soc.* **2014**, *136*, 11874-11877.
43. Harrop, T. C.; Tonzetich, Z. J.; Reisner, E.; Lippard, S. J. Reactions of Synthetic [2Fe-2S] and [4Fe-4S] Clusters with Nitric Oxide and Nitrosothiols. *J. Am. Chem. Soc.* **2008**, *130*, 15602-15610.
44. Tonzetich, Z. J.; Do, L. H.; Lippard, S. J. Dinitrosyl Iron Complexes Relevant to Rieske Cluster Nitrosylation. *J. Am. Chem. Soc.* **2009**, *131*, 7964-7965.
45. Victor, E.; Lippard, S. J. A Tetranitrosyl [4Fe–4S] Cluster Forms En Route to Roussin's Black Anion: Nitric Oxide Reactivity of $[Fe_4S_4(LS3)L']^{2-}$. *Inorg. Chem.* **2014**, *53*, 5311-5320.

46. Harrop, T. C.; Song, D.; Lippard, S. J. Reactivity pathways for nitric oxide and nitrosonium with iron complexes in biologically relevant sulfur coordination spheres. *J. Inorg. Biochem.* **2007**, *101*, 1730-1738.
47. Pal, N.; Majumdar, A. Transfer of Hydrosulfide from Thiols to Iron(II): A Convenient Synthetic Route for Nonheme Diiron(II)-hydrosulfide Complexes. *Dalton Trans.* **2019**, *48*, 5903-5908.
48. Ganguly, T.; Das, A.; Majumdar, A. Iron(II) Mediated Desulfurization of Organosulfur Substrates Produces Nonheme Diiron(II)-hydrosulfides. *Inorg. Chem.* **2019**, *58*, 9998-10011.
49. McKee, V.; Zvagulis, M.; Dagdigian, J. V.; Patch, M. G.; Reed, C. A. Hemocyanin Models-Synthesis, Structure, and Magnetic Properties of a Binucleating Copper(II) System. *J. Am. Chem. Soc.* **1984**, *106*, 4765-4772.
50. Armarego, W. L. F.; Chai, C. L. L. *Purification of Laboratory Chemicals*. Sixth ed.; Butterworth-Heinemann, Elsevier Inc.: USA, 2009.
51. Arulsamy, N.; Bohle, D. S.; Butt, J. A.; Irvine, G. J.; Jordan, P. A.; Sagan, E. Interrelationships between Conformational Dynamics and the Redox Chemistry of S-Nitrosothiols. *J. Am. Chem. Soc.* **1999**, *121*, 7115-7123.
52. Pal, N.; Majumdar, A. Controlling the Reactivity of Bifunctional Ligands: Carboxylate-Bridged Nonheme Diiron(II) Complexes Bearing Free Thiol Groups. *Inorg. Chem.* **2016**, *55*, 3181-3191.
53. Bill, E. julX, Program for Simulation of Molecular Magnetic Data; Max-Planck Institute for Chemical Energy Conversion: Mülheim/ Ruhr, Germany, 2008.
54. White, C. J. Modelling Flavodiiron Nitric Oxide Reductases: Geometric and Electronic Structure of Key Intermediates and Mechanistic Insights. PhD Thesis, University of Michigan, Ann Arbor, MI, USA, 2020.
55. *APEX II* 2009 Ed.; Bruker Analytical X-ray Systems Inc.: Madison, WI, 2009.
56. Spek, A. L. Single-crystal structure validation with the program PLATON. *J. Appl. Crystallogr.* **2003**, *36*, 7-13.
57. Spek, A. L. Structure validation in chemical crystallography. *Acta Crystallogr. Sect. D* **2009**, *65*, 148-155.
58. Sheldrick, G. M. A short history of SHELX. *Acta Crystallogr. Sect. A* **2008**, *64,* 112-122.
59. Dolomanov, O. V.; Bourhis, L. J.; Gildea, R. J.; Howard, J. A. K.; Puschmann, H. OLEX2: a complete structure solution, refinement and analysis program. *J. Appl. Crystallogr.* **2009**, *42*, 339-341.
60. Farrugia, L. J. ORTEP-3 for Windows - a version of ORTEP-III with a Graphical User Interface (GUI). *J. Appl. Crystallogr.* **1997**, *30*, 565.
61. Farrugia, L. J. WinGX and ORTEP for Windows: an update. *J. Appl. Crystallogr.* **2012**, *45*, 849-854.
62. Schlegel, H. B. S., G. E.; Scalmani, G.; Barone, V.; Mennucci, B.; Caricato, M.; Li, X.; Hratchian, H. P.; Hada, M.; Fukuda, R.; Hasegawa, J.; Ishida, M.; Nakajima, T.; Nakai, H.; Vreven, T.; Montgomery, J. A., Jr; Bearpark, M.; Keith, T.; Kobayashi, R.; Normand, J.; Burant, J. C.; Iyengar, S. S.; Tomasi, J.; Millam, J. M.; Klene, M.; Knox, J. E.; Cross, J. B.; Jaramillo, J.; Gomperts, R.; Stratmann, R. E.; Cammi, R.; Pomelli, C.; Ochterski, J. W.; Zakrzewski, V. G.; Voth, G. A.; Dapprich, S.; Daniels, A. D.; Ortiz, J. V.; Cioslowski, J.; Fox, D. J.; et al. Gaussian 09, Revision E.01; Wallingford, CT, 2013.
63. Becke, A. D. Density-functional thermochemistry. III. The role of exact exchange. *J. Chem. Phys.* **1993**, 5648-5652.
64. Lee, C.; Yang, W.; Parr, R. G. Development of the ColleSalvetti correlation-energy formula into a functional of the electron density. *Phys. Rev. B: Condens. Matter Mater. Phys.* **1988**, *37*, 785-789.

65. Perdew, J. P.; Burke, K.; Wang, Y. Generalized gradient approximation for the exchange-correlation hole of a many-electron system. *Phys. Rev. B: Condens. Matter Mater. Phys.* **1996**, *54*, 16533-16539.
66. Wachters, A. J. H. Gaussian Basis Set for Molecular Wavefunctions Containing Third-Row Atoms. *J. Chem. Phys.* **1970**, *52*, 1033-1036.
67. Hay, P. J. Gaussian basis sets for molecular calculations. The representation of 3d orbitals in transition-metal atoms. *J. Chem. Phys.* **1977**, 4377-4384.
68. Neese, F. Software update: the ORCA program system, version 4.0. *Wiley Interdiscip. Rev. Comput. Mol. Sci.* **2018**, *8*, p e1327.
69. Weigend, F. Accurate Coulomb-fitting basis sets for H to Rn. *Phys. Chem. Chem. Phys.* **2006**, *8*, 1057-1065.
70. Hunt, A. P.; Lehnert, N. The Thiolate Trans Effect in Heme $\{FeNO\}^6$ Complexes and Beyond: Insight into the Nature of the Push Effect. *Inorg. Chem.* **2019**, *58*, 11317-11332.
71. Hunt, A. P.; Samanta, S.; Dent, M. R.; Milbauer, M. W.; Burstyn, J. N.; Lehnert, N. Model Complexes Elucidate the Role of the Proximal Hydrogen-Bonding Network in Cytochrome P450s. *Inorg. Chem.* **2020**, *59*, 8034-8043.
72. McQuilken, A. C.; Ha, Y.; Sutherlin, K. D.; Siegler, M. A.; Hodgson, K. O.; Hedman, B.; Solomon, E. I.; Jameson, G. N. L.; Goldberg, D. P. Preparation of Non-heme $\{FeNO\}^7$ Models of Cysteine Dioxygenase: Sulfur versus Nitrogen Ligation and Photorelease of Nitric Oxide. *J. Am. Chem. Soc.* **2013**, *135*, 14024-14027.
73. Chiang, C.-Y.; Miller, M. L.; Reibenspies, J. H.; Darensbourg, M. Y. Bismercaptoethanediazacyclooctane as a N_2S_2 Chelating Agent and Cys−X−Cys Mimic for Fe(NO) and $Fe(NO)_2$. *J. Am. Chem. Soc.* **2004**, *126*, 10867-10874.
74. McQuilken, A. C.; Matsumura, H.; Dürr, M.; Confer, A. M.; Sheckelton, J. P.; Siegler, M. A.; McQueen, T. M.; Ivanović-Burmazović, I.; Moënne-Loccoz, P.; Goldberg, D. P. Photoinitiated Reactivity of a Thiolate-Ligated, Spin-Crossover Nonheme {FeNO}7 Complex with Dioxygen. *J. Am. Chem. Soc.* **2016**, *138*, 3107-3117.
75. Ekanayake, D. M.; Fischer, A. A.; Elwood, M. E.; Guzek, A. M.; Lindeman, S. V.; Popescu, C. V.; Fiedler, A. T. Nonheme iron–thiolate complexes as structural models of sulfoxide synthase active sites. *Dalton Trans.* **2020**, *49*, 17745-17757.
76. Feig, A. L.; Bautista, M. T.; Lippard, S. J. A Carboxylate-Bridged Non-Heme Diiron Dinitrosyl Complex. *Inorg. Chem.* **1996**, *35*, 6892-6898.
77. Majumdar, A.; Lippard, S. J. Non-Heme Mononitrosyldiiron Complexes: Importance of Iron Oxidation State in Controlling the Nature of the Nitrosylated Products. *Inorg. Chem.* **2013**, *52*, 13292-13294.
78. Berto, T. C.; Hoffman, M. B.; Murata, Y.; Landenberger, K. B.; Alp, E. E.; Zhao, J.; Lehnert, N. Structural and Electronic Characterization of Non-Heme Fe(II)–Nitrosyls as Biomimetic Models of the FeB Center of Bacterial Nitric Oxide Reductase. *J. Am. Chem. Soc.* **2011**, *133*, 16714-16717.
79. Speelman, A. L.; White, C. J.; Zhang, B.; Alp, E. E.; Zhao, J.; Hu, M.; Krebs, C.; Penner-Hahn, J.; Lehnert, N. Non-heme High-Spin $\{FeNO\}^{6-8}$ Complexes: One Ligand Platform Can Do It All. *J. Am. Chem. Soc.* **2018**, *140*, 11341-11359.
80. Van Stappen, C.; Lehnert, N. Mechanism of N–N Bond Formation by Transition Metal–Nitrosyl Complexes: Modeling Flavodiiron Nitric Oxide Reductases. *Inorg. Chem.* **2018**, *57*, 4252-4269.

SYNOPSIS TOC

A monohydrosulfido dinitrosyl diiron complex with [hs- (HS){FeNO}^{7}/ hs-{FeNO}^{7}] formulation produces N_2O in relation with flavodiiron nitric oxide reductases following a semireduction mechanism in which the coordinated hydrosulfide acts as a spectator ligand.